Reduced interdecadal variability of Atlantic Meridional Overturning Circulation under global warming

Jun Cheng[a,1], Zhengyu Liu[b,c,d,1], Shaoqing Zhang[e], Wei Liu[f], Lina Dong[a], Peng Liu[a], and Hongli Li[a]

[a]Polar Climate System and Global Change Laboratory, Nanjing University of Information Science & Technology, Nanjing 210044, China; [b]Department of Atmospheric and Oceanic Sciences, University of Wisconsin-Madison, Madison, WI 53706; [c]Nelson Center for Climatic Research, University of Wisconsin-Madison, Madison, WI 53706; [d]Laboratory for Climate and Ocean-Atmosphere Studies, School of Physics, Peking University, Beijing 100871, China; [e]Geophysical Fluid Dynamics Laboratory, National Oceanic and Atmospheric Administration, Princeton University, Princeton, NJ 08542; and [f]Scripps Institution of Oceanography, University of California, San Diego, La Jolla, CA 92037

Edited by Mark H. Thiemens, University of California, San Diego, La Jolla, CA, and approved February 9, 2016 (received for review October 6, 2015)

Interdecadal variability of the Atlantic Meridional Overturning Circulation (AMOC-IV) plays an important role in climate variation and has significant societal impacts. Past climate reconstruction indicates that AMOC-IV has likely undergone significant changes. Despite some previous studies, responses of AMOC-IV to global warming remain unclear, in particular regarding its amplitude and time scale. In this study, we analyze the responses of AMOC-IV under various scenarios of future global warming in multiple models and find that AMOC-IV becomes weaker and shorter with enhanced global warming. From the present climate condition to the strongest future warming scenario, on average, the major period of AMOC-IV is shortened from ∼50 y to ∼20 y, and the amplitude is reduced by ∼60%. These reductions in period and amplitude of AMOC-IV are suggested to be associated with increased oceanic stratification under global warming and, in turn, the speedup of oceanic baroclinic Rossby waves.

Atlantic Meridional Overturning Circulation | interdecadal variability | global warming | oceanic stratification | Rossby wave

As a modulator of low-frequency climate variation in the North Atlantic region (1–5), interdecadal variability of the Atlantic Meridional Overturning Circulation (AMOC-IV) has likely undergone significant changes in the past (6). Despite past efforts (7–9), responses of AMOC-IV to global warming remain unclear, in particular regarding the amplitude and period of AMOC-IV.

Here, we investigate the responses of AMOC-IV to future global warming in the state-of-the-art Coupled Model Intercomparison Project Phase 5 (CMIP5) simulations (10). We compare AMOC-IV in the future projection simulations of four warming scenarios of different Representative Concentration Pathways (RCPs, namely, RCP26, RCP45, RCP60, and RCP85; *Models and Experiments*) with AMOC-IV in the preindustrial (PI) control simulations. Five models are selected based on the criterion that each has at least two sufficiently long RCP simulations of up to the year 2300 (Table S1). With two or more long RCP simulations by each model, we can assess transient AMOC-IV responses among different scenarios with reasonable statistical significance. In the PI simulations, all models give significant AMOC-IV (Fig. S1*A* and *Definition of the AMOC Intensity*), exhibiting robust periods within the range of 10–100 y (Fig. S2). Under future global warming, the mean transport of the AMOC is reduced, with the ensemble mean ranging from being reduced by 5% in RCP26 to being reduced by 48% in RCP85 in the years 2100–2300 (Fig. S1 *B* and *D*), qualitatively consistent with Intergovernmental Panel on Climate Change studies (11).

Responses of AMOC-IV to Future Global Warming

In response to future global warming, AMOC-IV shows a robust change, with its major period shortened and its amplitude reduced. This can be seen in the analysis of the projected AMOC-IV in the 200-y window of years 2100–2300. Compared with the analysis with longer windows or using the entire time series in the PI simulations, the 200-y window can provide a reasonable estimation of the dominant features of AMOC-IV (Fig. S2). We first filter out the long-term background change of the AMOC from AMOC-IV in the RCP simulations using the method of Empirical Mode Decomposition (EMD) (12) (Fig. S3 *A–E* and *Identification of Interdecadal Variability*). In response to global warming, AMOC-IV is changed significantly across all of the models with respect to the PI simulations (Fig. S3 *F–J*). With the global warming intensifying from RCP26 to RCP85, AMOC-IV tends to have a shorter period and a smaller amplitude, especially for the stronger warming scenarios. This can be seen most clearly in the ensemble mean of the AMOC-IV power spectrum (Fig. 1 and *Power Spectral Analysis and Major Period/Amplitude of AMOC-IV*). Similar results can be found when a simple running mean is used to remove the long-term AMOC changes (Fig. S4).

As global warming intensifies, the ensemble mean of the major period of AMOC-IV (*Power Spectral Analysis and Major Period/Amplitude of AMOC-IV*) decreases from 57 y in the PI simulation to 54 y, 45 y, 29 y, and 15 y in RCP26, RCP45, RCP60, and RCP85, respectively (Fig. 2*A*, black dots). For each scenario, this ensemble mean major period is obtained as follows. First, the major period is obtained in each individual model; second, all of the major periods in different models are averaged. Compared with the cross-model sampling errors of AMOC-IV periods (42–72 y) assessed in the PI simulations (Fig. S1*A* and Fig. S2), the shortening of AMOC-IV periods in the stronger warming cases (RCP60 and RCP85) is statistically significant.

The amplitude of AMOC-IV, as measured by the power in the major period band (*Power Spectral Analysis and Major Period/Amplitude*

Significance

The Atlantic Meridional Overturning Circulation (AMOC) is a key component of the climate system, and its interdecadal variability (IV) significantly modulates climate changes around the North Atlantic region and worldwide. We report a robust shortening in period and weakening in amplitude of AMOC-IV in response to future global warming, which may be contributed to by increased oceanic stratification and, in turn, speedup of Rossby wave propagation. This finding sheds light on the mechanism of AMOC-IV responses to varying background climatology and global warming and therefore should contribute significantly to our understanding and projection of future climate changes.

Author contributions: J.C., Z.L., and S.Z. designed research; J.C. and W.L. performed research; L.D., P.L., and H.L. analyzed data; J.C. and Z.L. wrote the paper; and Z.L., S.Z., and W.L. interpreted the results.

The authors declare no conflict of interest.

This article is a PNAS Direct Submission.

Freely available online through the PNAS open access option.

[1]To whom correspondence may be addressed. Email: chengjun@nuist.edu.cn or zliu3@wisc.edu.

This article contains supporting information online at www.pnas.org/lookup/suppl/doi:10.1073/pnas.1519827113/-/DCSupplemental.

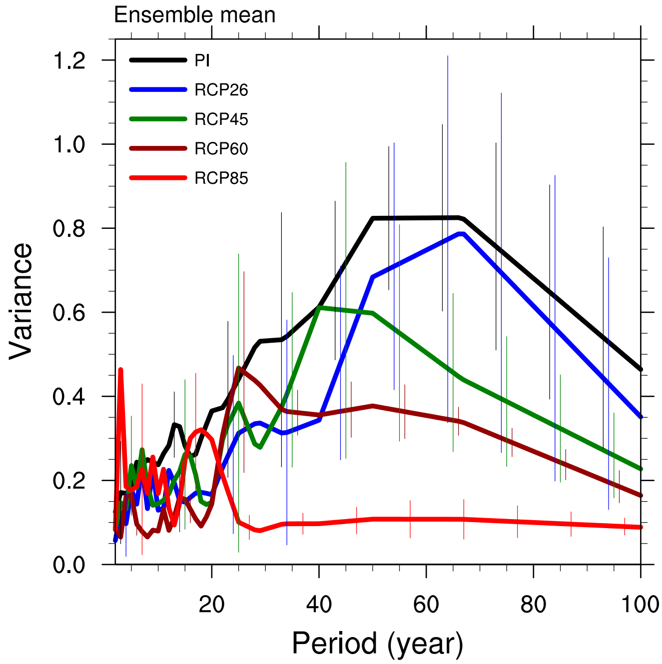

Fig. 1. Cross-model ensemble mean interdecadal variability of AMOC-IV from simulations of the PI and four projected global warming scenarios. The ensemble mean power spectrum (PS) curves of AMOC-IV of five models are for the PI simulation and four projected global warming scenarios (RCP26, RCP45, RCP60, and RCP85) in black, blue, dark green, brown, and red, respectively. The vertical lines over each PS indicate cross-model SD.

of AMOC-IV), tends to decrease with intensified warming. This is evident in the ensemble mean of variance ratio of AMOC-IV between the warming scenarios and the PI case (Fig. 2*B*, blue dots). The ensemble mean of variance ratio decreases by about 7%, 24%, 43%, and 60% for RCP26, RCP45, RCP60, and RCP85, respectively. The mean amplitude of AMOC-IV in the period band of 10–100 y also shows a robust decreasing trend (Fig. 2*C*, green dots).

The decreases in both amplitude and period of AMOC-IV under global warming can also be seen in each individual model, albeit with a larger spread than in the cross-model ensemble mean discussed above, especially for the cases of weak warming scenarios (Fig. 3). The large spread for each individual model is expected, because of the strong internal variability sampled in a 200-y window (Fig. S2). Under weak warming scenarios (RCP26 and RCP45), the responses of AMOC-IV can be distorted by the internal variability. Nevertheless, the shortening in period and weakening in amplitude of AMOC-IV are clear under stronger warming scenarios (RCP60 and RCP85) even in individual models (beyond the sampling error derived from the PI simulations). Regardless of the changes of AMOC-IV under different warming scenarios in each individual model, Fig. 3 illustrates that, across the models, there is a systematic trend of a stronger amplitude accompanied by a longer period of AMOC-IV. The correlation between the changes of amplitude and period is as high as 0.7, which is above the 99% significance level (whereas the amplitude increases from −71% to 33% with respect to the mean, and the period increases from 12 y to 70 y).

The reduced amplitude of AMOC-IV in response to global warming is consistent with several modeling studies (7–9). The time scale of AMOC-IV was suggested to have changed significantly in the past based on climate reconstructions (6). The responses of the time scale of AMOC-IV to future global warming, to our knowledge, have not been studied systematically.

It is interesting to note that, in contrast to the significant weakening of AMOC-IV, there is no clear trend in the amplitude of AMOC variability at the interannual time scale (Fig. 2*C*, purple dots). This seems to suggest that the dynamics for the amplitude of AMOC variability differ at different time scales, and the weakening of AMOC-IV is not simply a weakening proportional to that of the mean AMOC across all of the time scales (Fig. S1 *B* and *D*).

Mechanism of the AMOC-IV Changes

Various mechanisms have been proposed for the genesis of AMOC-IV (see the reviews in refs. 1 and 13–17). AMOC-IV has been proposed to be generated by stochastic atmospheric variability (18), planetary wave instability (19), or thermohaline instability (20). The oscillation behavior of AMOC-IV has been proposed to be associated with the phase lag between the salt and heat advection (21–27), the zonal and meridional temperature gradients [thermal Rossby wave (28–33)], and the meridional density gradient and advective flux [delayed advective oscillator (34)]. In many previous works, the time scale of AMOC-IV is proposed to be

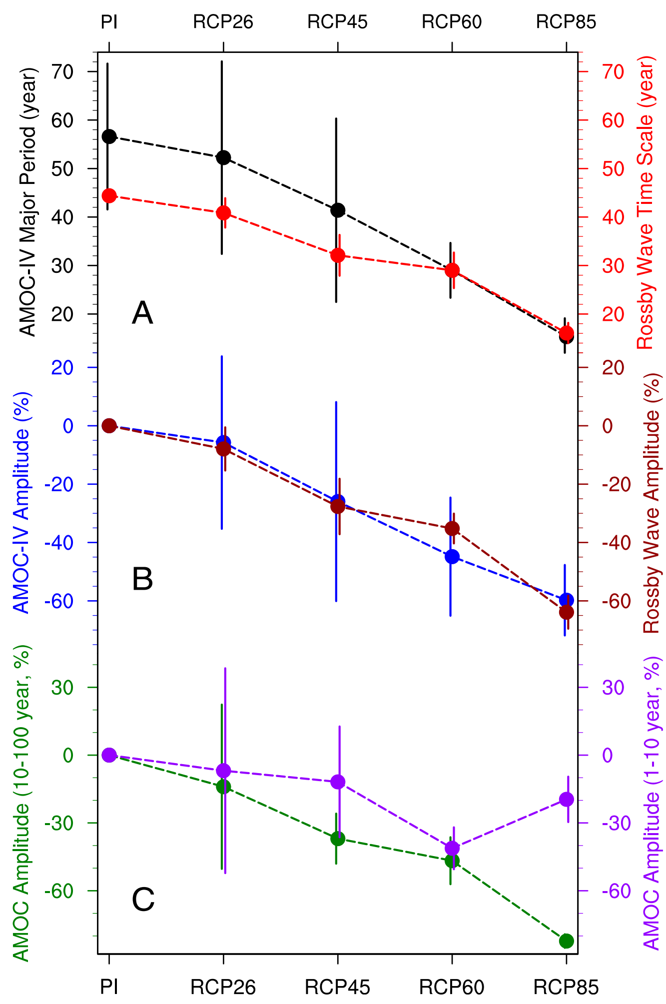

Fig. 2. Ensemble mean changes of AMOC-IV and baroclinic Rossby wave from the PI simulation to each of the projected global warming scenarios. (*A*) The major periods of AMOC-IV (black dots) and time scales of the first baroclinic Rossby wave propagation across the high-latitude North Atlantic (40°N–60°N, red dots). (*B*) The amplitude ratio (normalized by the PI amplitude) of AMOC-IV (blue dots) and the first baroclinic Rossby wave (brown dots) in each projected global warming scenario. (*C*) The amplitude ratio of AMOC variability averaged over interdecadal time scale (10–100 y, green dots) and over interannual time scale (1–10 y, purple dots). The PI ratio is subtracted in *B* and *C*. In *A*–*C*, the vertical line over each dot shows cross-model SD.

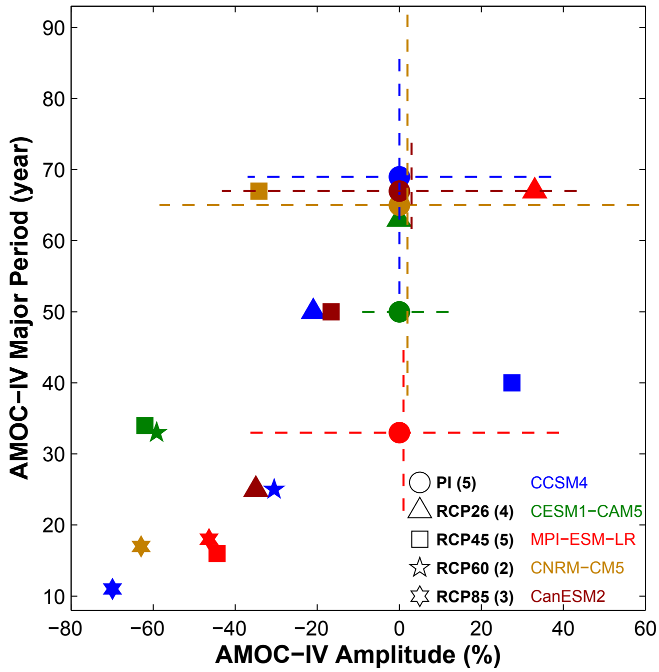

Fig. 3. Major periods and amplitudes of AMOC-IV from the PI simulation to each projected global warming scenario in individual models. A specific color is used for each model, and a unique marker is used for each experiment. Dashed lines over the PI dots show the sampling errors of AMOC-IV major period and amplitude in each individual model, which are derived as the SD of the major periods and amplitudes in multiple 200-y windows of the long PI simulations.

determined by the propagation of oceanic baroclinic Rossby waves (34–39) and/or thermal Rossby wave (28–33) across the basin.

Our preliminary analysis suggests that the full responses of AMOC-IV to global warming cannot be explained simply by previous mechanisms. For example, under global warming, there is neither a significant northward shift of the convection center (9) (Fig. S5) nor a significant change of the Arctic sea ice (27), especially under strong global warming. The latitudinal temperature gradient in the upper North Atlantic is increased, but by less than 43% (see Fig. S6). The implied speedup of thermal Rossby wave (28–30), if it is important, falls far short of explaining the 280% reduction of the major period of AMOC-IV (Fig. 2*A*). Therefore, a systematic study is needed to fully understand the response of AMOC-IV to global warming.

One candidate mechanism for the AMOC-IV responses, we suggest, is the oceanic baroclinic Rossby waves. The establishment and variability of the AMOC are accomplished by a basin-wide adjustment of oceanic density field in the North Atlantic, with the adjustment time scale determined primarily by the propagation of Rossby waves across the basin (35, 36), especially in high latitudes (37–39). With global warming, oceanic stratification is projected to be enhanced over the globe owing to a weaker warming with depth (40), and the stratification enhancement is more robust in a stronger warming scenario (11). A stronger stratification should lead to faster baroclinic Rossby waves and, potentially, a shorter period of AMOC-IV.

Here, the AMOC-IV in all of the models is associated with density anomalies mainly in high latitudes (40°N–60°N) of the North Atlantic (Fig. S7). Global warming increases oceanic stratification and, in turn, the buoyancy frequency (N^2) in the upper ocean of the high-latitude North Atlantic (Fig. S8). This leads to an acceleration of baroclinic Rossby waves, as calculated in each individual model under different scenarios. The wave speed is calculated from the eigenvalue problem in a linearized quasi-geostrophic potential vorticity equation, with the buoyancy frequency derived from the area mean N^2 profiles of the high-latitude North Atlantic (see *Supporting Information*). The most striking feature of the eigenvalues is an increase of wave speed with intensified global warming, whereas the eigenfunction structure remains largely unchanged (Fig. S9). The increased wave speed then reduces the cross-basin time scale of Rossby waves, as seen in the ensemble mean wave speed (Fig. 2*A*, red dots). This reduction of cross-basin time scale is largely consistent with the shortening of the major period of AMOC-IV (Fig. 2*A*, black dots). This wave calculation, although very crude, is consistent with the speculation that the shortening of the AMOC-IV major period could be contributed by the faster propagation of baroclinic Rossby waves in the midlatitude and high-latitude North Atlantic associated with strengthened stratification.

The mechanism for the weakening of AMOC-IV seems even more complex. This weakening does not seem to be caused by the weakening of stochastic atmospheric forcing, because the amplitude of atmospheric forcing on AMOC-IV remains nearly unchanged under global warming, as seen in the amplitude of the North Atlantic Oscillation that is the dominant atmospheric internal variability over the North Atlantic (Fig. S10). The weakening of AMOC-IV is also in contrast to the AMOC variability at higher frequencies, notably at the interannual time scale; the latter exhibits less clear weakening signals under global warming (Fig. 2*C*, purple dots). A further study is needed to understand the amplitude response to global warming. Here, we speculate on two mechanisms that may contribute to the weakening of AMOC-IV, both related to the speedup of Rossby waves. First, for the very low frequency variability like AMOC-IV, we may assume a quasi-stationary oceanic response to atmospheric forcing. Then, the amplitude of forced baroclinic Rossby wave response is inversely proportional to its wave speed, and therefore the cross-basin time scale (see *Supporting Information*). As a result, the amplitude weakens with the speedup of Rossby waves in response to global warming. This explains the reduction of variance ratio of the baroclinic Rossby wave under global warming (Fig. 2*B*, brown dots), which resembles closely that of AMOC-IV amplitude, both decreasing by ∼60% from the PI simulation to RCP85 (Fig. 2*B*, blue dots). Second, the weakening of AMOC-IV may also be interpreted from a nonlinear delayed oscillator perspective (34). As the Rossby wave speeds up, the delay time of the negative feedback diminishes, so that the delayed negative feedback becomes direct damping, and therefore reduces the instantaneous growth rate; in turn, the amplitude of AMOC-IV is reduced (see *Supporting Information* and Fig. S11).

Our study suggests that AMOC-IV may be significantly weakened in amplitude and shortened in period under future global warming, and that these responses could be caused by strengthened ocean stratification and, in turn, the speedup of baroclinic Rossby waves. Our results shed light on the responses of interdecadal variability to global warming and may help improve future predictions of climate changes at the interdecadal time scale.

Materials and Methods

Models and Experiments. We analyzed 19 experiments from five models in the CMIP5 archive (10), and each experiment has one preindustrial (PI) control simulation and four future warming scenarios (Table S1). The PI simulation uses the fixed forcing at the year 1850. Four simulations of future global warming scenarios are used, which are forced according to RCP26, RCP45, RCP60, and RCP85 (additional radiative forcing of 2.6 W·m^{-2}, 4.5 W·m^{-2}, 6.0 W·m^{-2}, and 8.5 W·m^{-2}, respectively, near year 2100, relative to the PI forcing). All potential density and pressure at sea level were regridded to a 1° × 1° grid before analysis. Different periods of the RCP simulations are used for the EMD method (period of 2100–2300) and the running mean method (period of 2050–2250). The entire period of the PI simulation in each model is used. Annual mean data are used in all of the analyses.

Definition of the AMOC Intensity. The intensity of the AMOC is defined as the maximum overturning streamfunction below 500 m in the Atlantic.

Identification of Interdecadal Variability. Interdecadal variability is identified using the Fast Fourier Transform (41) in power spectrum (42) after filtering out the variability longer than 100 y. In the simulations of different warming scenarios, the long-term trends are removed with the EMD method (12) (or with a high-pass 100-y running mean).

Power Spectral Analysis and Major Period/Amplitude of AMOC-IV. The long PI simulation is separated into a batch of 200-y windows with a 150-y overlay in adjacent windows (Fig. S1*A*). The power spectrum of each 200-y window and its mean are calculated for comparison with the results of the RCP experiments (years 2100–2300).

The cross-window ensemble mean power spectrum (for the 200-y window) can capture the major period of AMOC-IV (about 70 y or shorter), which is derived from longer windows, including the entire time series (Fig. S2). This implies that most of the 200-y windows are sufficient for the detection of the dominant features of AMOC-IV. In some cases, the lower variance for the major period of AMOC-IV is caused by the coarse period/frequency resolution at the interdecadal scale.

The ensemble mean power spectrum for each scenario is performed after being normalized by the spectral peak of the PI simulation of each model, so that the variance ratio between each warming scenario and the PI case is comparable among different models.

For each model, the major period and amplitude of AMOC-IV for an RCP simulation are defined by the spectral peak of the 200-y window of 2100–2300, whereas those for the PI simulation are calculated as the arithmetic mean of the spectra of all of the 200-y windows, instead of the spectrum of the entire PI simulation (although the two are similar). The cross-model ensemble mean spectrum is the mean of the spectra across different models.

ACKNOWLEDGMENTS. We thank Drs. H.-J. Yang, K. Fraedrich, H. Dijkstra, and X.-Y. Shen for valuable discussions, and Drs. Y. G. Liu and W. Zhang at Geophysical Fluid Dynamics Laboratory for their useful comments on an early version of the manuscript. We acknowledge the World Climate Research Programme's Working Group on Coupled Modelling, which is responsible for Coupled Model Intercomparison Project, and we thank the climate modeling groups for producing and making available their model outputs. This work is supported by the National Basic Research Program of China (Grants 2012CB955200 and 2015CB953902) and the National Natural Science Foundation of China (Grants 41206024 and 41130105).

1. Latif M, et al. (2006) A review of predictability studies of Atlantic sector climate on decadal time scales. *J Clim* 19(23):5971–5987.
2. Frankignoul C, et al. (2013) The influence of the AMOC variability on the atmosphere in CCSM3. *J Clim* 26(24):9774–9790.
3. Enfield DB, Mestas-Nunez AM, Trimble PJ (2001) The Atlantic Multidecadal Oscillation and its relation to rainfall and river flows in the continental U. S. *Geophys Res Lett* 28(10):2077–2080.
4. Folland CK, Palmer TN, Parker DE (1986) Sahel rainfall and worldwide sea temperatures, 1901–85. *Nature* 320:602–607.
5. Sutton RT, Hodson DLR (2005) Atlantic Ocean forcing of North American and European summer climate. *Science* 309(5731):115–118.
6. Hertzberg JE, et al. (2012) Decadal- to centennial-scale tropical Atlantic climate variability across a Dansgaard-Oeschger cycle. *Paleoceanography* 27(3):PA3218.
7. Bryan FO, et al. (2006) Response of the North Atlantic Thermohaline Circulation and ventilation to increasing carbon dioxide in CCSM3. *J Clim* 19(11):2382–2397.
8. Ortega P, et al. (2012) Variability of the Atlantic Meridional Overturning Circulation in the last millenium and two IPCC scenarios. *Clim Dyn* 38(9):1925–1947.
9. Drijfhout S, et al. (2008) Future changes in internal variability of the Atlantic Meridional Overturning Circulation. *Clim Dyn* 30(4):407–419.
10. Taylor KE, Stouffer RJ, Meehl GA (2012) An overview of the CMIP5 and the experimental design. *Bull Am Meteorol Soc* 93(4):485–498.
11. Collins M, et al. (2013) Long-term climate change: Projections, commitments and irreversibility. *Climate Change 2013: The Physical Science Basis*, eds Stocker TF, et al. (Cambridge University Press, Cambridge, UK), pp 1029–1136.
12. Huang NE, Long SR, Shen Z (1996) The mechanism for frequency downshift in nonlinear wave evolution. *Adv Appl Mech* 32:59–111.
13. Latif M (1998) Dynamics of interdecadal variability in coupled ocean–atmosphere models. *J Clim* 11(4):602–624.
14. Miller AJ, Schneider N (2000) Interdecadal climate regime dynamics in the North Pacific Ocean: Theories, observations and ecosystem impacts. *Prog Oceanogr* 47: 355–379.
15. Xie SP, Carton JA (2004) Tropical Atlantic variability: Patterns, mechanisms, and impacts. *Earth Climate: The Ocean-Atmosphere Interaction*, Geophysical Monograph Series, eds Wang C, Xie SP, Carton JA (Am Geophys Union, Washington, DC), Vol 147, pp 121–142.
16. Delworth T, Zhang R, Mann M (2007) Decadal to centennial variability of the Atlantic from observations and models. *Ocean Circulation: Mechanisms and Impacts*, Geophysical Monograph Series, eds Schmittner A, Chiang JCH, Hemming SR (Am Geophys Union, Washington, DC), Vol 173, pp 131–148.
17. Liu Z (2012) Dynamics of interdecadal climate variability: A historical perspective. *J Clim* 25(6):1963–1995.
18. Delworth TL, Greatbatch RJ (2000) Multidecadal thermohaline circulation variability driven by atmospheric surface flux forcing. *J Clim* 13(9):1481–1495.
19. Huck T, Vallis GK, Colin de Verdiére A (2001) On the robustness of the interdecadal modes of the thermohaline circulation. *J Clim* 14(5):940–963.
20. Weaver A, Sarachik ES, Marotzke J (1991) Internal low frequency variability of the ocean's thermohaline circulation. *Nature* 353:836–838.
21. Griffies SM, Tziperman E (1995) A linear thermohaline oscillator driven by stochastic atmospheric forcing. *J Clim* 8(10):2440–2453.
22. Ruprich-Robert Y, Cassou C (2015) Combined influences of seasonal East Atlantic Pattern and North Atlantic Oscillation to excite Atlantic multidecadal variability in a climate model. *Clim Dyn* 44(1):229–253.
23. Danabasoglu G, et al. (2012) Variability of the Atlantic Meridional Overturning Circulation in CCSM4. *J Clim* 25(15):5153–5172.
24. Dong B, Sutton TR (2005) Mechanism of interdecadal thermohaline circulation variability in a coupled ocean–atmosphere GCM. *J Clim* 18(8):1117–1135.
25. Wouters B, Drijfhout S, Hazeleger W (2012) Interdecadal North-Atlantic meridional overturning circulation variability in EC-EARTH. *Clim Dyn* 39(11):2695–2712.
26. Timmermann A, et al. (1998) Northern Hemispheric interdecadal variability: A coupled air-sea mode. *J Clim* 11(8):1906–1931.
27. Hawkins E, Sutton R (2007) Variability of the Atlantic Thermohaline Circulation described by three-dimensional empirical orthogonal functions. *Clim Dyn* 29(7):745–762.
28. te Raa LA, Dijkstra HA (2002) Instability of the thermohaline ocean circulation on interdecadal timescales. *J Phys Oceanogr* 32(1):138–160.
29. Dijkstra HA, te Raa L, Schmeits M, Gerrits J (2006) On the physics of the Atlantic multidecadal oscillation. *Ocean Dyn* 56(1):36–50.
30. Sévellec F, Fedorov AV (2013) The leading, interdecadal eigenmode of the Atlantic Meridional Overturning Circulation in a realistic ocean model. *J Clim* 26(7):2160–2183.
31. Buckley MW, et al. (2012) On the relationship between decadal buoyancy anomalies and variability of the Atlantic Meridional Overturning Circulation. *J Clim* 25(23): 8009–8030.
32. MacMartin DG, Tziperman E, Zanna L (2013) Frequency domain multimodel analysis of the response of Atlantic Meridional Overturning Circulation to surface forcing. *J Clim* 26(21):8323–8340.
33. Frankcombe LM, Dijkstra HA, von der Heydt A (2008) Sub-surface signatures of the Atlantic Multidecadal Oscillation. *Geophys Res Lett* 35(19):L19602.
34. Lee SK, Wang C (2010) Delayed advective oscillation of the Atlantic thermohaline circulation. *J Clim* 23(5):1254–1261.
35. Kawase M (1987) Establishment of deep ocean circulation driven by deep-water production. *J Phys Oceanogr* 17(12):2294–2317.
36. Johnson H, Marshall D (2002) A theory for the surface Atlantic response to thermohaline variability. *J Phys Oceanogr* 32(4):1121–1132.
37. Liu Z (2002) How long is the memory of tropical ocean dynamics. *J Clim* 15(23): 3518–3522.
38. Liu Z (2003) Tropical ocean decadal variability and the resonance of planetary wave basin modes: I: Theory. *J Clim* 16(10):1539–1550.
39. Hristova H, Dijkstra HA, Spall M (2010) Onset of time-dependence in a double-gyre circulation: Barotropic basin modes versus classical baroclinic modes. *J Mar Res* 68(2): 215–236.
40. Capotondi A, et al. (2012) Enhanced upper ocean stratification with climate change in the CMIP3 models. *J Geophys Res* 117(C4):C04031.
41. Cooley JW, Tukey JW (1965) An algorithm for the machine calculation of complex Fourier series. *Math Comput* 19(90):297–301.
42. Akselrod S, et al. (1981) Power spectrum analysis of heart rate fluctuation: A quantitative probe of beat-to-beat cardiovascular control. *Science* 213(4504):220–222.
43. Gill AE (1982) *Atmosphere-Ocean Dynamics* (Academic, New York).
44. Suarez MJ, Schopf PS (1988) A delayed action oscillator for ENSO. *J Atmos Sci* 45(21): 3283–3287.

Supporting Information

Cheng et al. 10.1073/pnas.1519827113

SI Materials and Methods

Time Scale of Rossby Wave. The Rossby wave speed is calculated from the eigenvalue problem in the linearized quasi-geostrophic potential vorticity equation (43), with the buoyancy frequency (N^2) vertical profiles derived for each model's mean ocean state in the high-latitude North Atlantic (40°N–60°N),

$$\partial_t \left[\partial_z \left(\frac{f_0^2}{N^2} \partial_z \varphi \right) \right] + \beta \partial_x \varphi = 0$$

where $N^2 = -\frac{g}{\rho_0} \frac{d\rho}{dz}$, and φ denotes the streamfunction.

Set $\varphi = \phi(z) e^{i(kx - \omega t)}$,

$$\frac{d}{dz}\left(\frac{f_0^2}{N^2} \frac{d\phi}{dz} \right) - \lambda \phi = 0,\ \lambda = -\frac{\beta k}{\omega}. \qquad \textbf{[S1]}$$

The vertical boundary condition of no motion at the top and bottom reduces to

$$\left. \frac{d\phi}{dz} \right|_{z=0,D} = 0. \qquad \textbf{[S2]}$$

The buoyancy frequency N^2 in each experiment is interpolated to a uniform 5-m layer in the depth range of 4,000 m. A centered three-point finite difference scheme is used to solve the eigenvalue problem of Eqs. **S1** and **S2**. The finite difference form of the eigenvalue problem is therefore of the form

$$A \phi_m = \lambda_m \phi_m$$

where λ_m is the mth eigenvalue and ϕ_m is the mth eigenfunction. For specific values of f_0 and N_2, we can obtain the values of λ_m and ϕ_m. The phase speed of the first baroclinic Rossby wave is

$$c_1 = \frac{\omega}{k} = \frac{\beta}{\lambda_1}.$$

The time scale of the first baroclinic Rossby wave propagating from the east to the west in the latitude band of 40°N–60°N of the North Atlantic is

$$T = \frac{L}{c_1}$$

where L denotes the mean width of the North Atlantic between 40°N and 60°N and is set to 3,700 km. The application of the eigenvalue problem to different models shows that the wave speed increases rapidly with global warming (Fig. S9*A*) whereas the eigenfunction of the wave (Fig. S9 *B–F*) exhibits a typical first baroclinic mode structure.

It is worth noting that the domain of 40°N–60°N in the North Atlantic is selected here as a crude representation of the subpolar region where AMOC-IV is dominant (Fig. S7). The exact latitude of the Rossby wave that is relevant to the time scale of the AMOC-IV, if it exists, still remains to be explored. Here, however, the robust feature is the relative change of the wave speed with global warming, with a rapid speedup of ~200% (Fig. 2*A*). This feature is determined mainly by the change of stratification. In contrast to the stratification, the major latitude factor, f^2 in Eq. **S1**, although it affects the absolute magnitude of the wave speed, remains the same across different warming scenarios and therefore does not contribute directly to the relative change of the wave speed with global warming. Because the magnitude of the speedup due to stratification is roughly comparable to the shortening of the AMOC-IV (~280%, Fig. 2*A*), we speculate that the Rossby wave mechanism can be an important mechanism. Meanwhile, we note that it is likely that other mechanisms can also contribute to the shortening of the AMOC-IV, such as the latitudinal density change and the associated thermal Rossby wave, as discussed in the second paragraph of *Mechanism of the AMOC-IV Changes* (Fig. S6).

Amplitude of Rossby Wave. The weakening of the AMOC-IV may be interpreted in terms of forced Rossby wave. The equation for the Rossby wave forced by atmospheric forcing Q can be written as (43)

$$\partial_t \varphi + c_1 \partial_x \varphi = Q \qquad \textbf{[S3]}$$

where $\partial_x \varphi = v$ denotes the northward geostrophic velocity. For the low-frequency forcing case in which temporal variability is not dominant, we may have a quasi-stationary response $c_1 v \sim Q$. If the atmospheric forcing Q remains largely unchanged in response to global warming while the wave speed c_1 is accelerated, the amplitude of the forced response will be inversely proportional to the wave speed, or proportional to the cross-basin time scale, namely, $v \sim \frac{Q}{c_1} \sim QT$. Therefore, a faster wave also leads to a smaller amplitude of response, as long as the wave is not too fast to lead to a failure of the quasi-equilibrium response.

AMOC-IV Amplitude in Delayed Oscillator Perspective. The weakening of the AMOC-IV may also be interpreted from a nonlinear delayed oscillator (34) perspective. With global warming and the speedup of Rossby wave, the delay time is reduced such that the amplitude of the AMOC-IV is reduced monotonically as shown in Fig. S11. Indeed, this reduction of wave amplitude with wave delay can be calculated as a robust feature in a more general delayed oscillator model, such as that of Suarez and Schopf (44). Mechanistically, when the wave delay diminishes, the negative feedback associated with the delay becomes an instantaneous negative feedback that cancels the instantaneous growth rate, leading to a reduced amplitude of the oscillation.

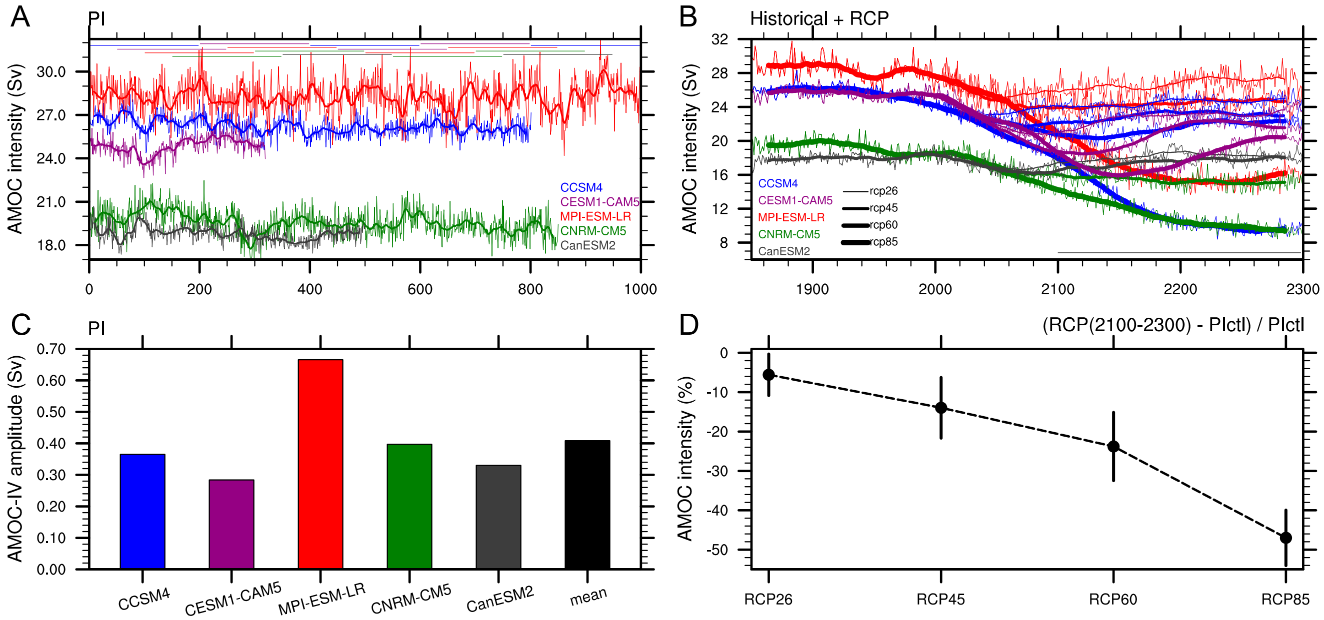

Fig. S1. AMOC intensity, AMOC-IV amplitude and long-term changes. AMOC intensity in the PI (*A*) and RCP (*B*) simulations. (*C*) SD of AMOC interdecadal variability (10–100 y) of each model in the PI simulation and their ensemble mean. (*D*) Ensemble mean of the amplitude ratio of AMOC intensity of each RCP simulation (averaged over the years 2100–2300) normalized by the PI case. Error bar shows the cross-model SDs in each RCP simulation. Horizontal lines in *A* and *B* show the 200-y windows for the PS analysis.

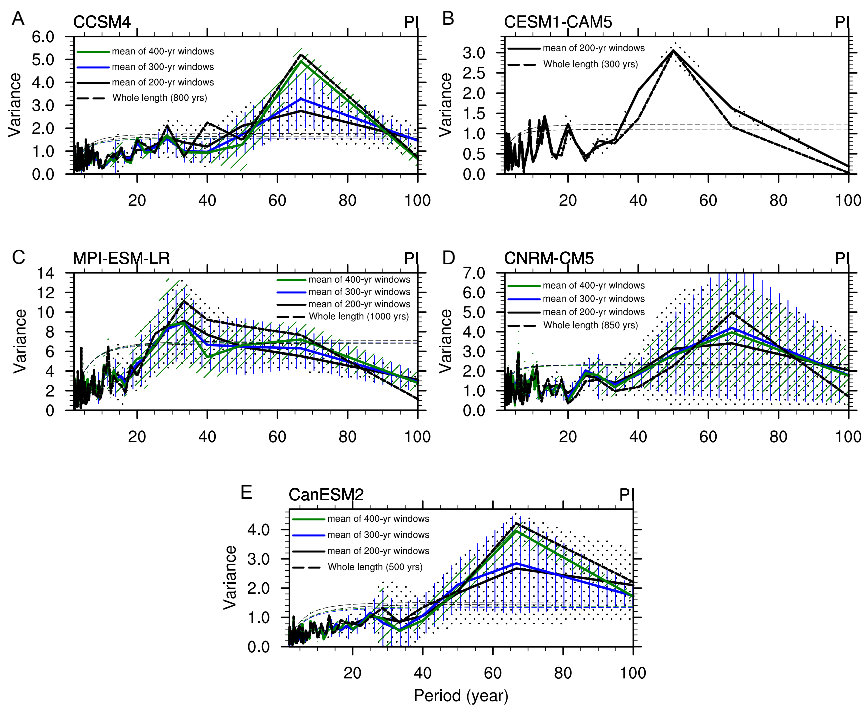

Fig. S2. Power spectrum of AMOC in the PI simulation. Shown are results for each of the five models: (*A*) CCSM4, (*B*) CESM1-CAM5, (*C*) MPI-ESM-LR, (*D*) CNRM-CM5, and (*E*) CanESM2. Cross-window ensemble mean power spectrum curves with different window lengths (200 y, 300 y, and 400 y) are shown as black, blue, and green solid lines, respectively, with the corresponding SDs marked as vertical bars of the same color. The power spectrum of the entire time series is shown as the dashed black curve.

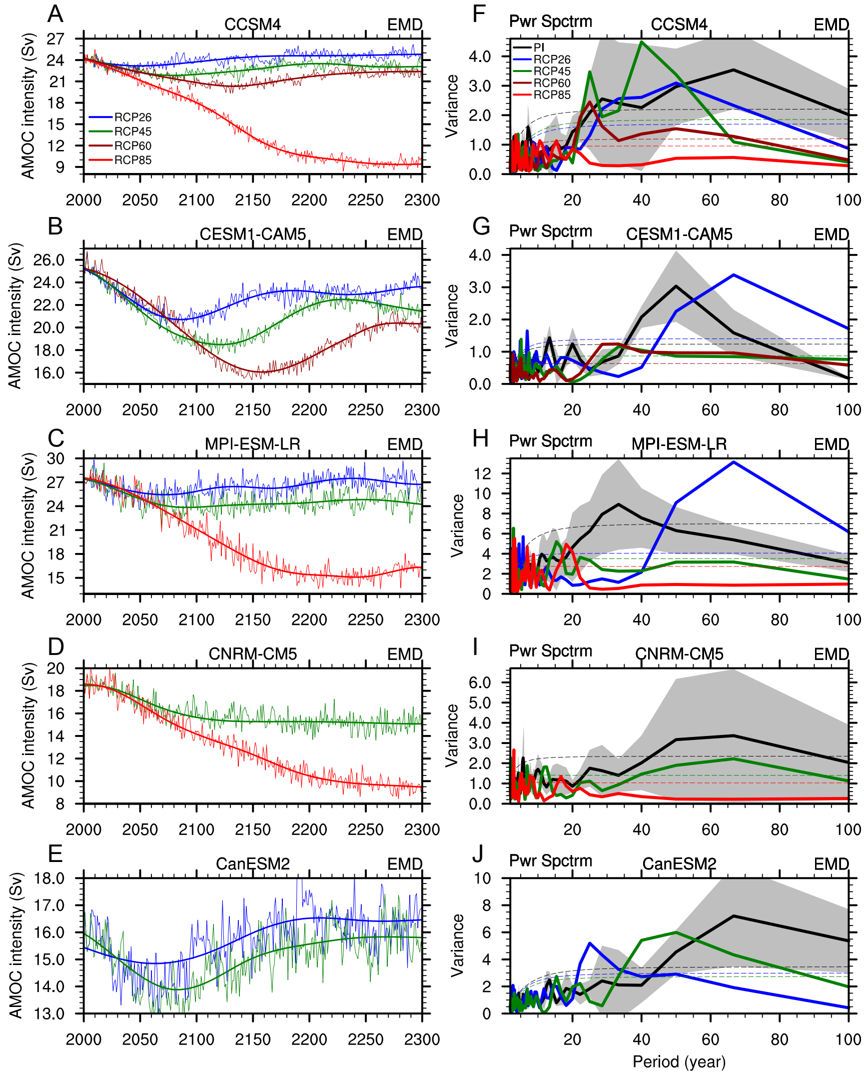

Fig. S3. Identification and power spectrum (Pwr Spctrm) of AMOC-IV. (*A*–*E*) AMOC intensity series (thin curves) and their long-term trends (derived using the EMD method, thicker curves) for the RCP simulations by each model. (*F*–*J*) Power spectrum of AMOC intensity in each model for the PI simulation (black curve) and RCP simulations in the years 2100–2300 after removing their long-term trends (color curves). The 95% confidence level of each power spectrum is labeled using a dashed curves. Cross-window SDs of the power spectrum in the long PI simulation are shown as gray shading. The PI power spectrum is derived as the mean of all of the 200-y windows. Models are (*A* and *F*) CCSM4, (*B* and *G*) CESM1-CAM5, (*C* and *H*) MPI-ESM-LR, (*D* and *I*) CNRM-CM5, and (*E* and *J*) CanESM2.

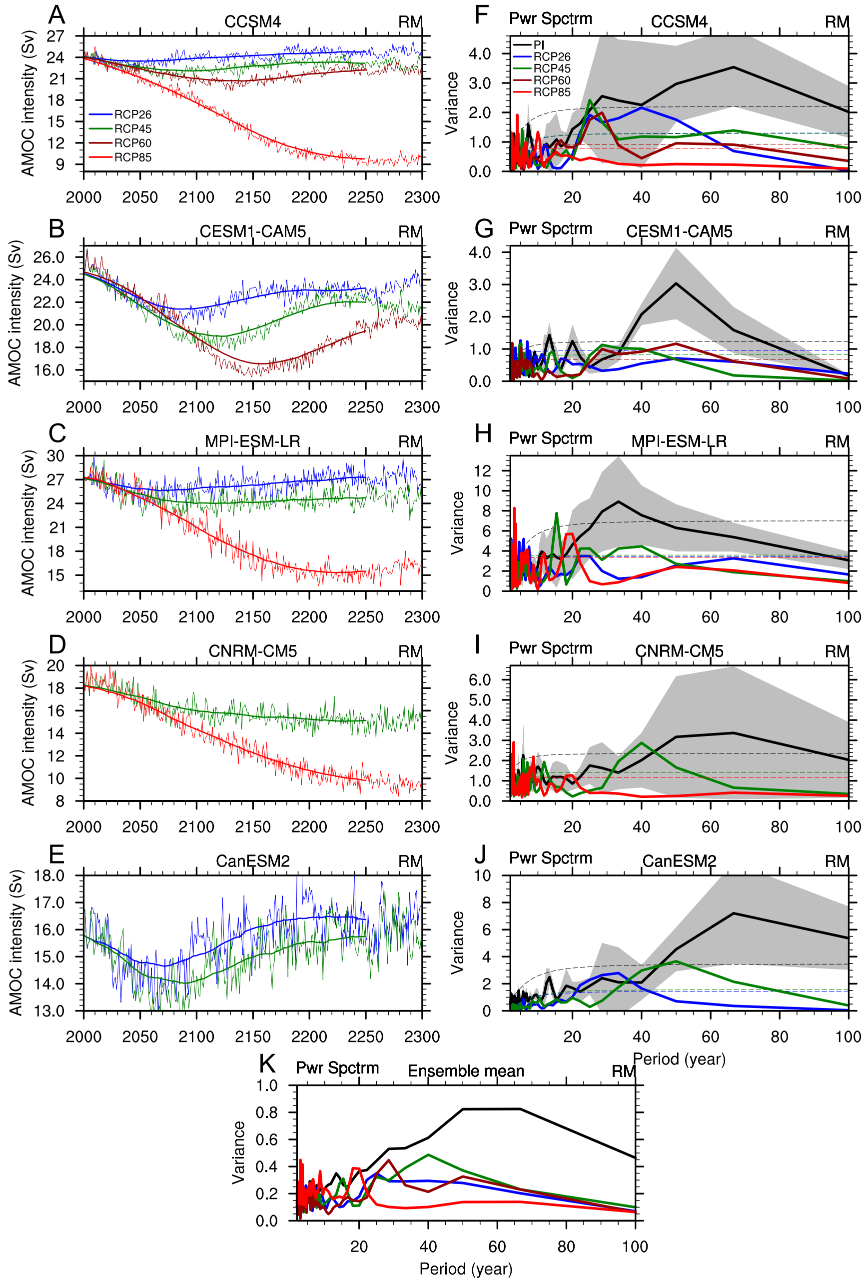

Fig. S4. (*A*–*J*) Same as Fig. S3, except using the low-pass filter of a 100-y running mean (RM) (instead of EMD). (*K*) Ensemble mean of the power spectrum. The power spectrum for each RCP simulation is performed for the years 2050–2250.

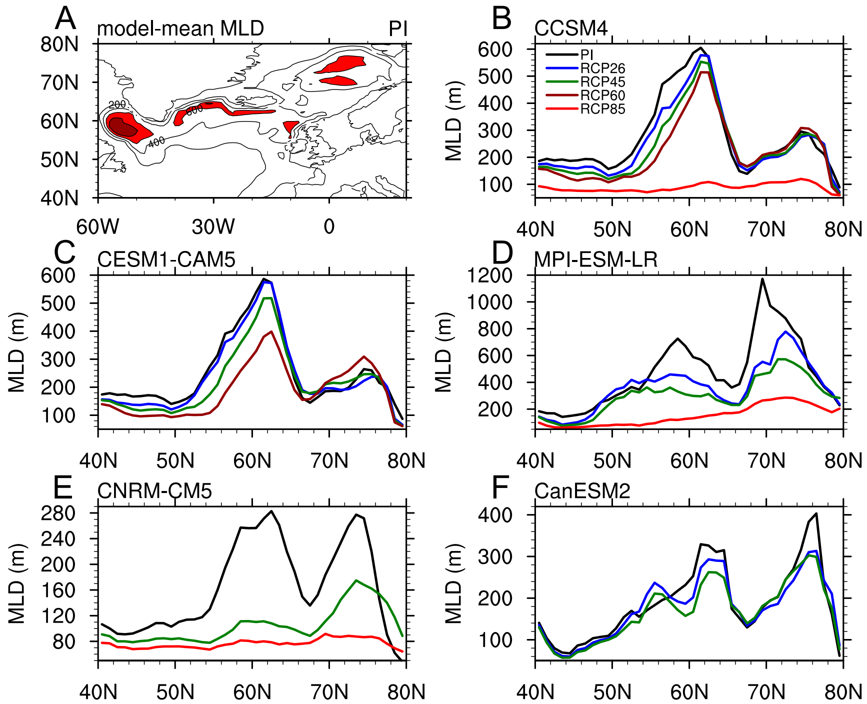

Fig. S5. Distribution of mixed layer depth in winter (December–February) and its changes under global warming. (*A*) Five-model mean mixed layer depth in winter in the PI simulation. (*B*–*F*) Zonal mean mixed layer depth (60°W–20°E) in the PI and RCP simulations for each model: (*B*) CCSM4, (*C*) CESM1-CAM5, (*D*) MPI-ESM-LR, (*E*) CNRM-CM5, and (*F*) CanESM2. There is no significant northward shift of mixed layer depth in winter under global warming.

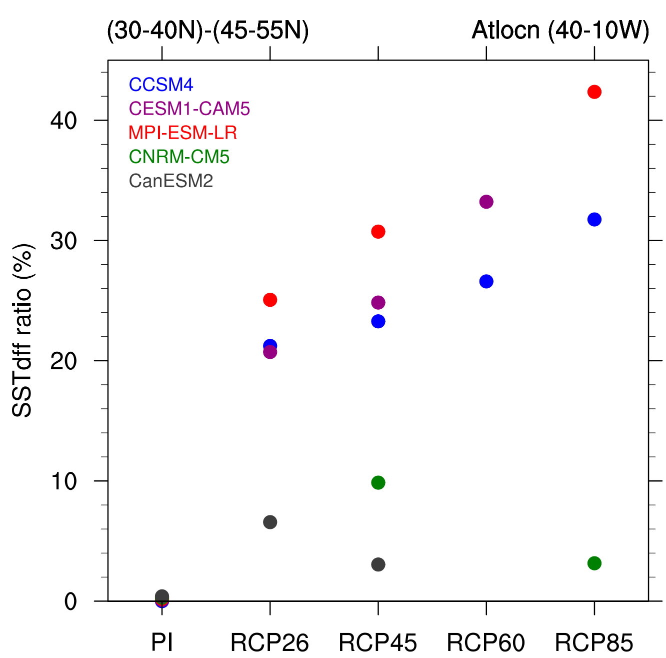

Fig. S6. Change ratio of meridional SST gradient (SST dff ratio) in the Atlantic of the RCP simulations compared with the value of the PI simulation for each model.

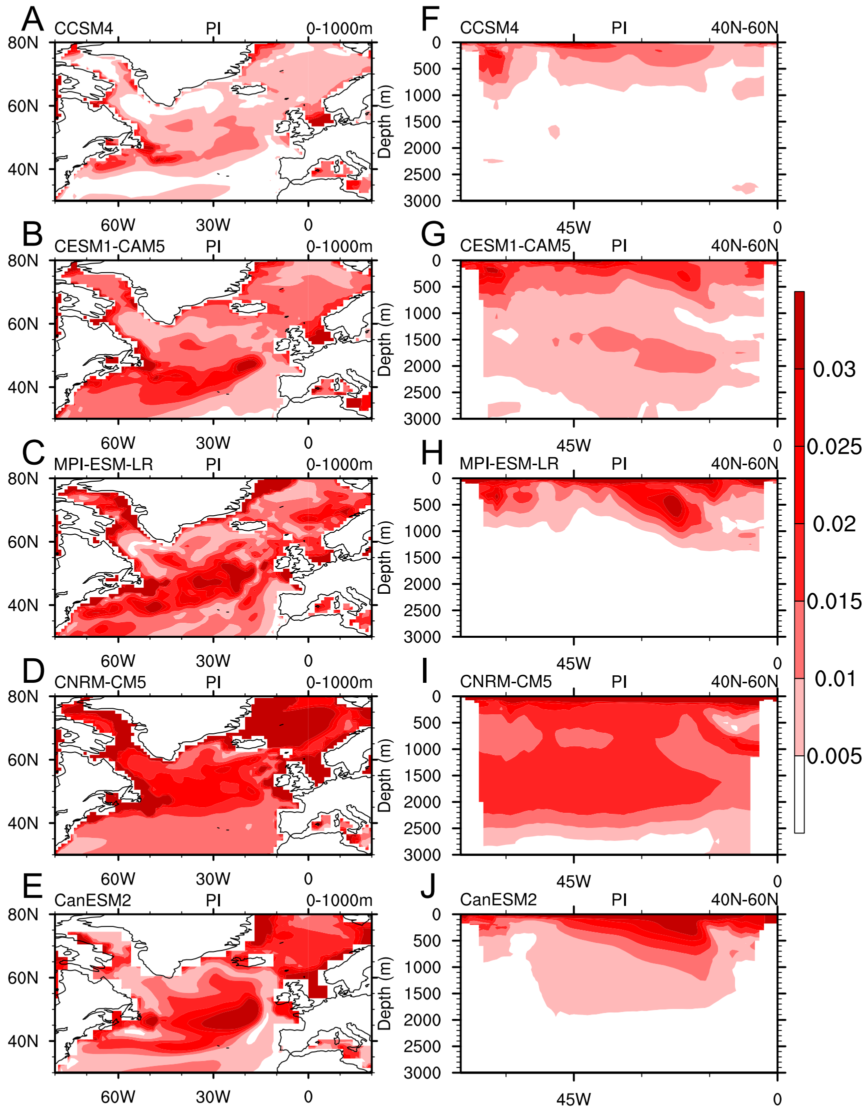

Fig. S7. Interdecadal (10–100 y) SD of oceanic potential density in the PI simulation. (*A*–*E*) Averaged in the depth range of the upper 1,000 m. (*F*–*J*) Averaged between 40°N and 60°N. Models are (*A* and *F*) CCSM4, (*B* and *G*) CESM1-CAM5, (*C* and *H*) MPI-ESM-LR, (*D* and *I*) CNRM-CM5, and (*E* and *J*) CanESM2. Units are kilogram per cubic meter.

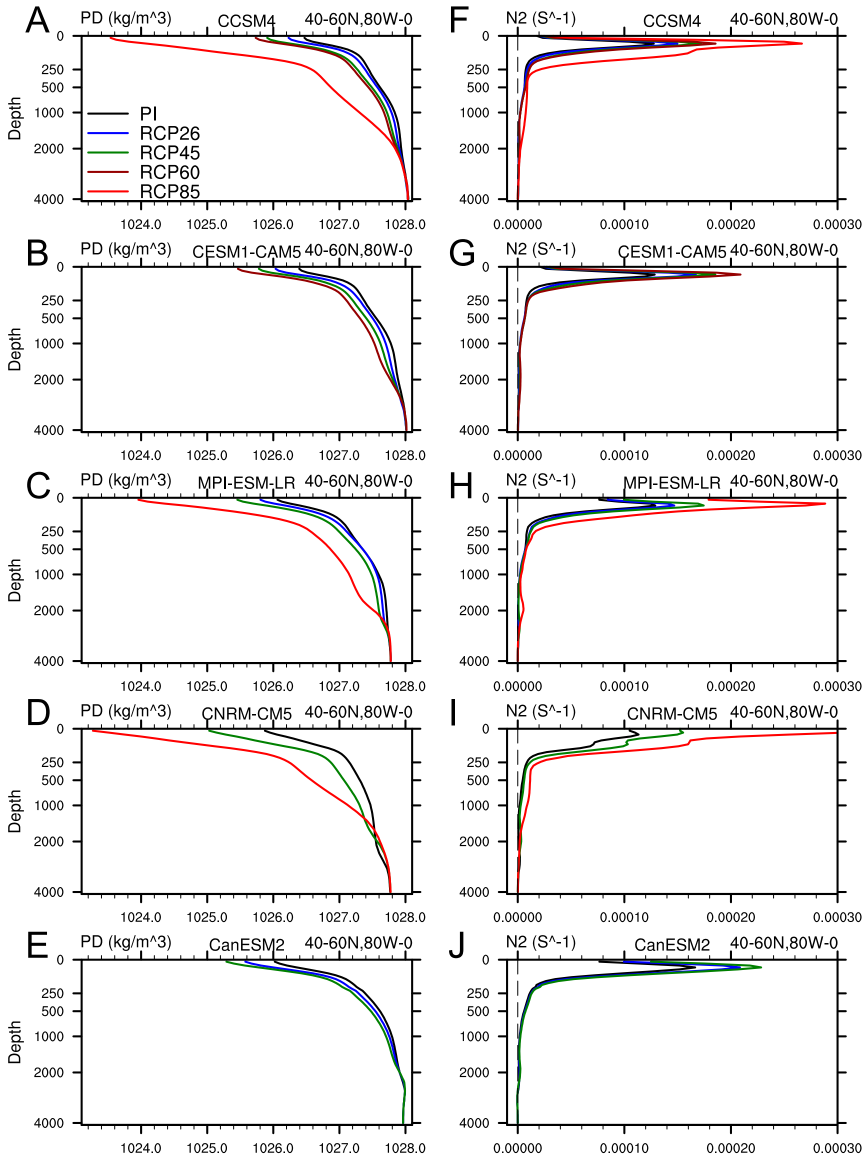

Fig. S8. Vertical profiles of area mean potential density and buoyancy frequency (N^2) of North Atlantic. (*A–E*) Potential density for each model and (*F–J*) N^2 for each model: (*A* and *F*) CCSM4, (*B* and *G*) CESM1-CAM5, (*C* and *H*) MPI-ESM-LR, (*D* and *I*) CNRM-CM5, and (*E* and *J*) CanESM2. Results of the PI and RCP simulations are shown as black, blue, dark green, brown, and red for PI, RCP26, RCP45, RCP60, and RCP85, respectively.

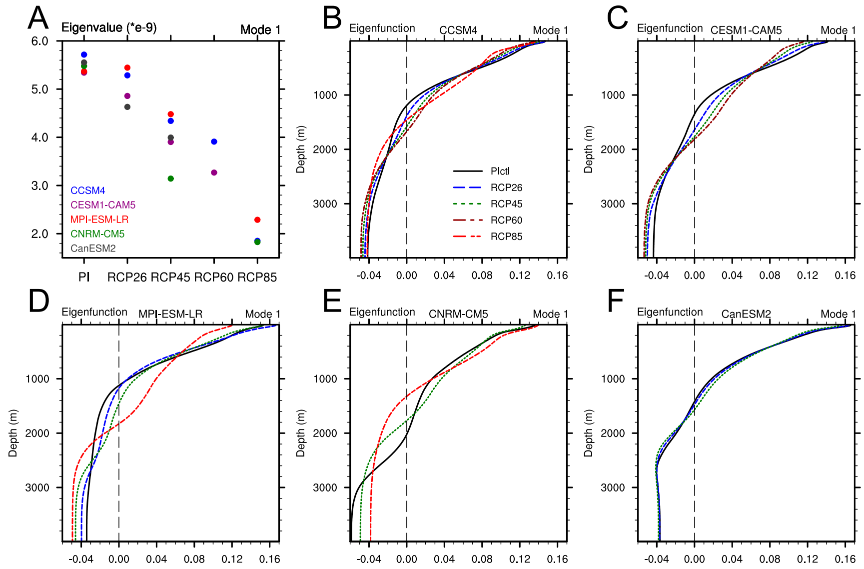

Fig. S9. Eigenvalue and eigenfunction of the first baroclinic Rossby wave. (*A*) Eigenvalues in the PI and RCP simulations of individual models. (*B*–*F*) Eigenfunctions in the PI and RCP simulations of individual models: (*B*) CCSM4, (*C*) CESM1-CAM5, (*D*) MPI-ESM-LR, (*E*) CNRM-CM5, and (*F*) CanESM2.

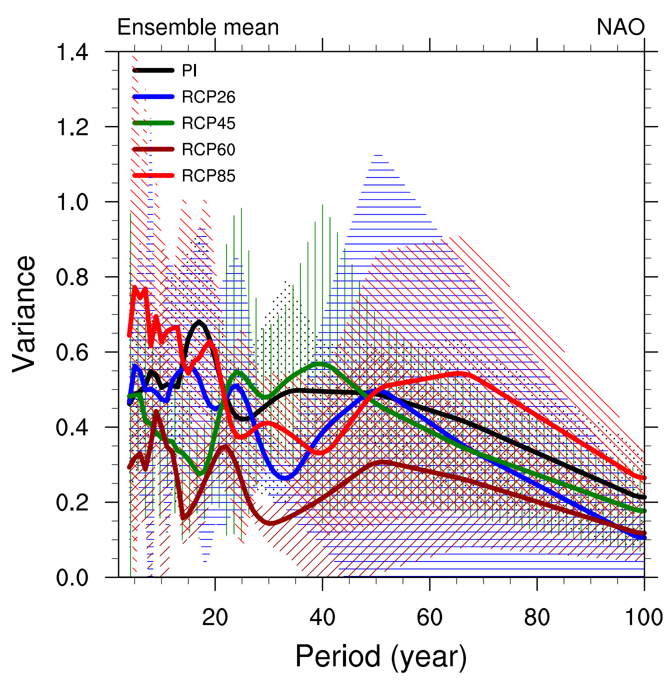

Fig. S10. Ensemble mean power spectrum of the North Atlantic Oscillation (NAO). The NAO index is defined as the difference of area mean sea level pressure between (90°W–60°E, 20°N–55°N) and (90°W–60°E, 55°N–90°N). The NAO does not show a systematic shift toward weaker amplitude and shorter period at the interdecadal time scale.

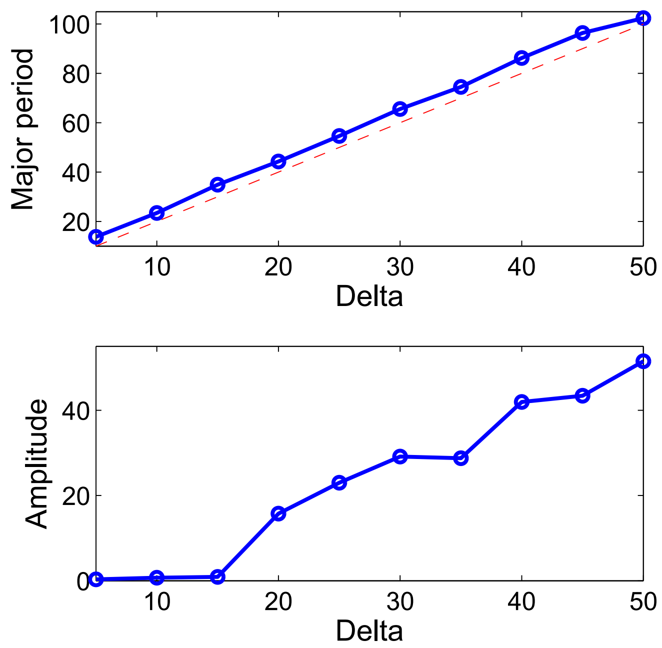

Fig. S11. Changes of major period and amplitude of circulation with respect to different delay times in a four-box ocean model with white noise forcing (34).

Table S1. Climate models and simulations

Model name	Country	PI	RCP26	RCP45	RCP60	RCP85
CCSM4	United States	Y	Y	Y	Y	Y
CESM1-CAM5	United States	Y	Y	Y	Y	
MPI-ESM-LR	Germany	Y	Y	Y		Y
CNRM-CM5	France	Y		Y		Y
CanESM2	Canada	Y	Y	Y		

"Y" indicates the simulation is used in this study.